



OGLE-2016-BLG-1469L: Microlensing Binary Composed of Brown Dwarfs

C. Han¹, A. Udalski^{2,22}, T. Sumi^{3,23}, A. Gould^{4,5,24}

and

M. D. Albrow⁶, S.-J. Chung^{4,7}, Y. K. Jung⁸, Y.-H. Ryu⁴, I.-G. Shin⁸, J. C. Yee⁸, W. Zhu⁵, S.-M. Cha^{4,9}, S.-L. Kim^{4,7}, D.-J. Kim⁴,
C.-U. Lee^{4,7}, Y. Lee^{4,9}, B.-G. Park^{4,7}

(The KMTNet Collaboration),

I. Soszyński², P. Mróz², P. Pietrukowicz², M. K. Szymański², J. Skowron², R. Poleski^{2,5}, S. Kozłowski², K. Ulaczyk², M. Pawlak²
(The OGLE Collaboration),

and

F. Abe¹⁰, Y. Asakura¹⁰, D. P. Bennett^{11,12}, I. A. Bond¹³, A. Bhattacharya¹², M. Donachie¹⁴, M. Freeman¹⁴, A. Fukui¹⁵, Y. Hirao¹⁶,
Y. Itow¹⁰, N. Koshimoto¹⁶, M. C. A. Li¹⁴, C. H. Ling¹³, K. Masuda¹⁰, Y. Matsubara¹⁰, Y. Muraki¹⁰, M. Nagakane¹⁶, K. Ohnishi¹⁷,
H. Oyokawa¹⁰, N. J. Rattenbury¹⁴, To. Saito¹⁸, A. Sharan¹⁴, D. J. Sullivan¹⁹, D. Suzuki^{11,12}, P. J. Tristram²⁰, T. Yamada³,
T. Yamada²⁰, A. Yonehara¹², R. Barry²¹

(The MOA Collaboration)

¹ Department of Physics, Chungbuk National University, Cheongju 28644, Korea² Warsaw University Observatory, Al. Ujazdowskie 4, 00-478 Warszawa, Poland³ Department of Earth and Space Science, Graduate School of Science, Osaka University, Toyonaka, Osaka 560-0043, Japan⁴ Korea Astronomy and Space Science Institute, Daejeon 34055, Korea⁵ Department of Astronomy, Ohio State University, 140 W. 18th Ave., Columbus, OH 43210, USA⁶ University of Canterbury, Department of Physics and Astronomy, Private Bag 4800, Christchurch 8020, New Zealand⁷ Korea University of Science and Technology, 217 Gajeong-ro, Yuseong-gu, Daejeon 34113, Korea⁸ Harvard-Smithsonian Center for Astrophysics, 60 Garden St., Cambridge, MA, 02138, USA⁹ School of Space Research, Kyung Hee University, Yongin 17104, Korea¹⁰ Institute for Space-Earth Environmental Research, Nagoya University, Nagoya 464-8601, Japan¹¹ Code 667, NASA Goddard Space Flight Center, Greenbelt, MD 20771, USA¹² Department of Physics, University of Notre Dame, 225 Nieuwland Science Hall, Notre Dame, IN 46556, USA¹³ Institute of Natural and Mathematical Sciences, Massey University, Auckland 0745, New Zealand¹⁴ Department of Physics, University of Auckland, Private Bag 92019, Auckland, New Zealand¹⁵ Okayama Astrophysical Observatory, National Astronomical Observatory of Japan, 3037-5 Honjo, Kamogata, Asakuchi, Okayama 719-0232, Japan¹⁶ Department of Earth and Space Science, Graduate School of Science, Osaka University, Toyonaka, Osaka 560-0043, Japan¹⁷ Nagano National College of Technology, Nagano 381-8550, Japan¹⁸ Tokyo Metropolitan College of Aeronautics, Tokyo 116-8523, Japan¹⁹ School of Chemical and Physical Sciences, Victoria University, Wellington, New Zealand²⁰ Mt. John University Observatory, P.O. Box 56, Lake Tekapo 8770, New Zealand²¹ Astrophysics Science Division, NASA Goddard Space Flight Center, Greenbelt, MD 20771, USA

Received 2017 April 9; revised 2017 May 15; accepted 2017 May 16; published 2017 July 3

Abstract

We report the discovery of a binary composed of two brown dwarfs, based on the analysis of the microlensing event OGLE-2016-BLG-1469. Thanks to the detection of both finite-source and microlens-parallax effects, we are able to measure both the masses $M_1 \sim 0.05 M_\odot$ and $M_2 \sim 0.01 M_\odot$, and the distance $D_L \sim 4.5$ kpc, as well as the projected separation $a_\perp \sim 0.33$ au. This is the third brown-dwarf binary detected using the microlensing method, demonstrating the usefulness of microlensing in detecting field brown-dwarf binaries with separations of less than 1 au.

Key words: binaries: general – brown dwarfs – gravitational lensing: micro

1. Introduction

Studies about brown dwarfs are important because the masses of brown dwarfs occupy the gap between the least massive stars and the most massive planets and thus they can provide important clues for understanding the formation mechanisms of both stars and planets (Basri 2000). In addition, brown dwarfs may be as abundant as stars in the Galaxy.

Considering that the multiplicity of stars is a ubiquitous result of the star-formation process, an important fraction of brown dwarfs may reside in binaries. Since the first discoveries by Rebolo et al. (1995) and Nakajima et al. (1995), there have been numerous discoveries of brown dwarfs. See the archives of brown-dwarf

candidates maintained by C. Gelino et al. (<http://DwarfArchives.org>) and J. Gagne. (<https://jgagneastro.wordpress.com/list-of-ultracool-dwarfs/>). However, the number of known binary systems composed of brown dwarfs, e.g., Luhman (2013) and Burgasser et al. (2013), is small.²⁵ The studies on the binary properties such as the binary frequency and the distributions of separations and mass ratios between binary components are important to probe the nature of brown dwarfs because these properties are influenced by both the process of the formation and dynamical interaction between the components within systems. Therefore, a sample composed of an increased number of binary brown-dwarf systems will be important to give shape to the details of the brown-dwarf formation process.

²² The OGLE Collaboration.

²³ The KMTNet Collaboration.

²⁴ The MOA Collaboration.

²⁵ There exist 52 brown-dwarf binaries among 1281 brown dwarfs listed in Gelino Catalog.

Microlensing can provide a useful tool to search for binary brown-dwarf systems, especially those that are difficult to detect using other methods. Due to their extremely low luminosities, detecting brown dwarfs using either the imaging or spectroscopic methods is restricted to those in nearby stellar associations within which brown dwarfs are young enough to emit observable light. By contrast, microlensing, which is caused by the gravity of an intervening object (lens) between an observer and a background star (source), occurs regardless of the lens brightness, and thus it can be used to detect old field brown-dwarf populations. Furthermore, while the spectroscopic measurement of a brown-dwarf mass is extremely difficult (Zapatero Osorio et al. 2004), the chance to measure the mass of a binary lens is relatively high, enabling us to make the brown-dwarf nature of the object definitive. The usefulness of the microlensing method has been demonstrated by the detections and the mass measurements of two field brown-dwarf binaries (Choi et al. 2013).

In this paper, we present the microlensing discovery of another binary system composed of brown dwarfs. Coverage of the caustic-approach region and the long timescale of the lensing event enables us to uniquely determine the mass of the lens system and thus to identify the substellar nature of the binary components.

The paper is organized as follows. In Section 2, we describe observations of the lensing event and the data acquired from them. In Section 3, we explain the detailed procedure of modeling the observed lensing light curve and present the solution of the lensing parameters. In Section 4, we present the physical parameters of the lens system. In Section 5, we discuss the nature of the low relative lens-source proper motion estimated from the light-curve analysis. We summarize the results of the analysis and conclude in Section 6.

2. Observation and Data

The brown-dwarf binary was discovered from the observation and analysis of the microlensing event OGLE-2016-BLG-1469. The source star of the event is located toward the Galactic bulge field with equatorial coordinates $(\alpha, \delta)_{J2000} = (18^{\text{h}}07^{\text{m}}46^{\text{s}}.98, -26^{\circ}17'23''.6)$, which correspond to the Galactic coordinates $(l, b) = (4^{\circ}.75, -2^{\circ}.92)$.

The lensing-induced brightening of the source star was first noticed on 2016 July 31 ($\text{HJD}' = \text{HJD} - 2450000 \sim 7600.5$) by the Early Warning System (EWS; Udalski 2003) of the Optical Gravitational Lensing Experiment (OGLE; Udalski et al. 2015). The OGLE lensing survey is conducted using the 1.3 m telescope located at the Las Campanas Observatory in Chile. The OGLE telescope is equipped with a 1.4 deg^2 field-of-view (FOV) camera. Most images of the OGLE data were taken in the standard Cousins *I* band with roughly 5% of observations in the Johnson *V* band for color measurement.

The event was also observed by the Microlensing Observations in Astrophysics (MOA; Bond et al. 2001; Sumi et al. 2003). The MOA survey uses the 1.8 m telescope at the Mt. John University Observatory in New Zealand. The MOA telescope is equipped with a 2.2 deg^2 FOV CCD camera. The MOA survey uses a customized wide *R*-band filter, where the wavelength range corresponds to the sum of the standard Cousins *R* and *I* bands. In the online list of MOA transient events, the lensing event was dubbed MOA-2016-BLG-542.

The event was also in the footprint of the Korea Microlensing Telescope Network (KMTNet; Kim et al. 2016) survey. The survey uses globally distributed three identical 1.6 m telescopes located at the Cerro Tololo Inter-American Observatory in Chile (KMTC), the South African Astronomical Observatory in South Africa (KMTS), and the Siding Spring Observatory in Australia (KMTA). A 4.0 deg^2 FOV camera is mounted on each of the KMTNet telescopes. Most of the KMTNet data were obtained in the standard Cousins *I*-band filter with occasional *V*-band observations.

Figure 1 shows the light curve of the lensing event OGLE-2016-BLG-1469 with the data taken by five telescopes of the three lensing surveys. Since the first discovery of the event by the OGLE group, the light curve continued to rise until a lensing magnification reached $A \sim 20$ at the peak ($\text{HJD} \sim 7646$). Covering the peak region of a high-magnification event is important because the efficiency to detect planetary signals is high (Griest & Safizadeh 1998). An anomalous signal actually occurred on $\text{HJD}' \sim 7646.5$ and the MOA group issued an anomaly alert to the microlensing community for possible follow-up observations. In the upper panel of Figure 1, we present the zoom of the anomaly. Responding to the alert, eight images were taken using two telescopes of the Las Cumbres Global Telescope Network. However, the coverage of the follow-up observation was too short (several hours) to give constraints on modeling the light curve and thus we do not use the data in the analysis. After the anomaly, the light curve gradually declined. Besides the central anomaly, the event is different from typical lensing events in the sense that the duration of the event is very long. The lensing-induced brightening of the source star started from the beginning of the 2016 bulge season and continued even after the end of the season.

Photometry of the data was conducted using codes based on the difference imaging method (Tomaney & Crofts 1996; Alard & Lupton 1998) and customized by the individual groups: Udalski (2003), Bond et al. (2001), and Albrow et al. (2009) for the OGLE, MOA, and KMTNet surveys, respectively. For the analysis of data taken by different telescopes and processed by different photometry codes, we normalize the error bars of the individual data sets following the usual procedure described in Yee et al. (2012), i.e.,

$$\sigma = k(\sigma_0^2 + \sigma_{\min}^2)^{1/2}. \quad (1)$$

Here σ_0 represents the error bar estimated from the photometry pipeline, σ_{\min} is a term used to adjust error bars so that error bars become consistent with their scatter, and k is a factor used to make the χ^2 per degree of freedom unity. The χ^2 value is calculated based on the best-fit solution of the lensing parameters obtained from modeling. In Table 1, we list the error-bar adjustment factors for the individual data sets.

3. Modeling Light Curve

When a lens is composed of two masses, the lens system induces a network of caustics at which the lensing magnification of a point source becomes infinity. Therefore, the light curve of a binary-lens event with a source trajectory that crosses or approaches close to the caustic results in deviations from the smooth light curve of a point-mass event. Caustics of a binary lens form a single or multiple set(s) of closed curves.

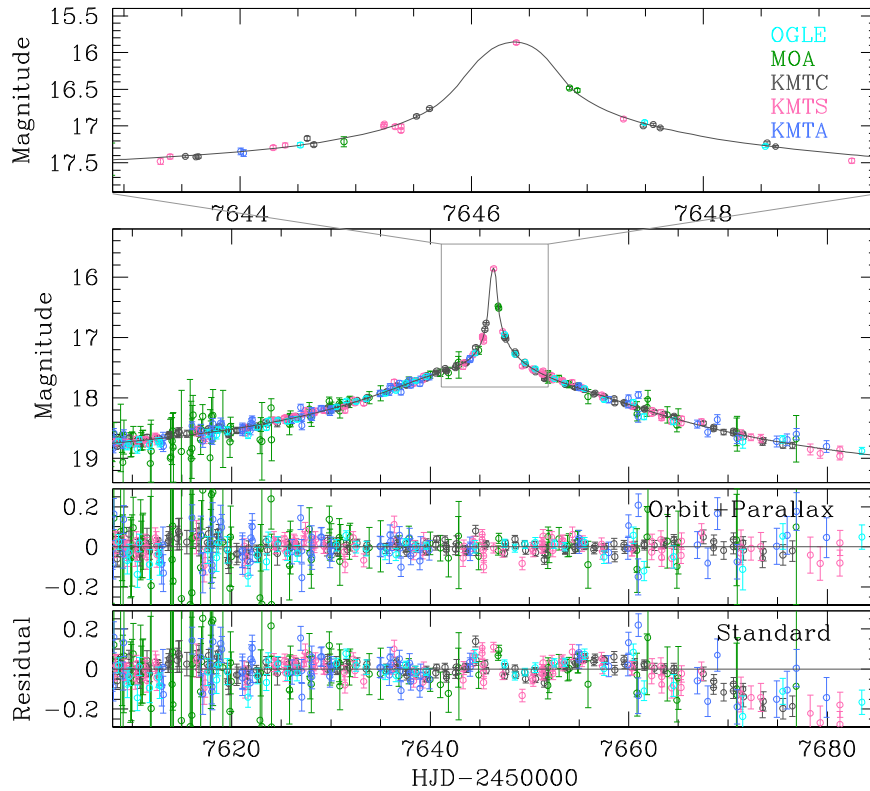


Figure 1. Light curve of the microlensing event OGLE-2016-BLG-1469. The upper panel shows the enlarged view of the anomaly around the peak. The two lower panels show the residual from the binary-lens models with (orbit+parallax) and without (standard) considering higher-order effects.

Table 1
Error-bar Adjustment Factors

Data set	k	σ_{\min}
OGLE	1.304	0.005
MOA	1.241	0.010
KMTC	1.044	0.010
KMTS	1.109	0.020
KMTA	1.572	0.020

A central anomaly in the lensing light curve of a high-magnification event occurs in two cases of binary lenses. The first case is a binary composed of roughly equal masses with a projected separation either substantially smaller (close binary) or larger (wide binary) than the angular Einstein radius θ_E . For a close binary, there exist three sets of caustics where one is located around the barycenter of the binary lens and the other two are located away from the center of mass. Then, a central anomaly of a high-magnification event occurs when a source passes close to the central caustic. For a wide binary, on the other hand, there exist two sets of caustics located close to the individual lens components. In this case, a central anomaly occurs when a source approaches either of the two caustics. The other binary-lens case producing central anomalies is a binary composed of two masses with extreme mass ratios, e.g., star-planet systems. In this case, the low-mass lens component induces a small caustic near the high-mass lens component and the central perturbation occurs when the source passes close to the caustic around the high-mass component.

Knowing the possible causes of central anomalies, we search for a solution of the binary-lens parameters that best describe the observed lensing light curve. Under the assumption that the

relative lens-source motion is rectilinear, the light curve of a binary-lens event is described by seven principle parameters. These parameters include the time of the closest source approach to a reference position of the lens, t_0 , the lens-source separation at that moment, u_0 (impact parameter), and the timescale for a lens to cross the Einstein radius, t_E (Einstein timescale), the projected lens-source separation normalized to θ_E , s , the mass ratio between the lens components, q , the angle between the source trajectory and the binary-lens axis, α (source-trajectory angle), and the ratio of the angular source radius θ_* to the angular Einstein radius, $\rho = \theta_*/\theta_E$ (normalized source radius). We note that the normalized source radius is needed to account for finite-source effects that occur when the source approaches a caustic. For the reference position on the lens plane, we use the barycenter for a close-binary lens and the photocenter for a wide-binary lens. The photocenter is located on the binary axis with an offset $q/[s(1+q)]$ from each lens component (An & Han 2002).

Since the central anomaly is likely to be produced by the source approach close to a caustic, we consider light-curve variation caused by finite-source effects. We compute finite-source magnifications by applying both numerical and semi-analytic approaches. In the numerical approach, we use the ray-shooting method. In this method, a large number of rays are uniformly shot from the image plane, bent according to the lens equation, and gathered on the source plane. With the map of rays on the source plane, the finite-source magnification for a given source position is computed as the number density ratio of rays on the source surface to the density on the image plane. The ray-shooting method is computer intensive. To accelerate computation, we compute magnifications in the vicinity of the regions around caustics using the semi-analytic hexadecapole approximations

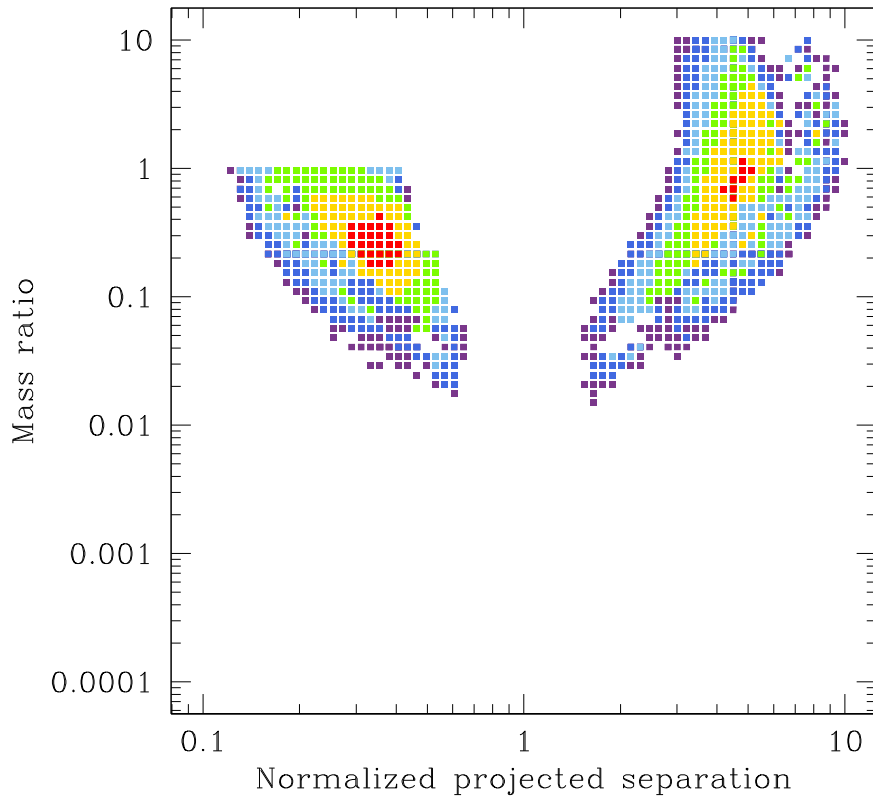


Figure 2. $\Delta\chi^2$ map of the MCMC chain in the parameter space of the projected separation s and the mass ratio q between the binary components. Color coding represents the regions with $\Delta\chi^2 < n$ (red), $4n$ (yellow), $9n$ (green), $16n$ (cyan), $25n$ (blue), and $36n$ (purple), where $n = 4$.

Table 2
Comparison of Models

Model		χ^2	
		Close	Wide
Standard		1849.0	1778.8
Parallax	$(u_0 > 0)$	1384.5	1396.1
	$(u_0 < 0)$	1385.2	1395.7
Orbit+Parallax	$(u_0 > 0)$	1380.3	1393.4
	$(u_0 < 0)$	1381.0	1393.0

(Gould 2008; Pejcha & Heyrovský 2009). In computing finite magnifications, we take account of the limb-darkening effects of the source star by using the model of the surface brightness profile $S_\lambda \propto 1 - \Gamma_\lambda(1 - 3 \cos \phi/2)$, where ϕ is the angle between the light of sight toward the center of mass and the normal to the source surface. The limb-darkening coefficients Γ_λ are adopted from Claret (2000) considering the stellar type of the source star. See Section 4 for the procedure to decide the source type. The adopted coefficients are $\Gamma_I = 0.45$ and $\Gamma_V = 0.62$. For the non-standard MOA filter, we adopt a mean value between R and I band, i.e., $\Gamma_{\text{MOA}} = 0.53$.

Searching for solutions of the lensing parameters is conducted in multiple steps. In the first step, we conduct a dense grid search over the (s, q, α) parameter space while other parameters are searched for using a downhill approach. We choose s , q , and α as grid parameters because lensing magnifications vary sensitively to small changes of these parameters, while the magnification variation to the changes of the other parameters is smooth. We use the Markov Chain Monte Carlo (MCMC) method for the downhill approach. This

preliminary search provides local minima in the parameter space. In the second step, we refine the individual local solutions first by narrowing down the grid space and then allowing all parameters to vary. In the final step, we find a global solution by comparing a χ^2 value of the local solutions. Considering that the central perturbation in the light curve of OGLE-2016-BLG-1469 can be produced by either a close/wide binary or a planetary companion, we set the ranges of s ($-1.0 < \log s < 1.0$) and q ($-5.0 < \log q < 1.0$) wide enough to investigate both possibilities.

In the initial modeling based on the principal parameters (standard model), we find no solution that can adequately describe the observed light curve, especially the asymmetric feature of the light curve. See the residual of the standard model presented in the bottom panel of Figure 1. Considering that the duration of the event comprises a significant portion of the Earth's orbital period, the deviation of the lens-source relative motion from rectilinear could be significant enough to cause long-term deviations in the lensing light curve, i.e., the parallax effect (Gould 1992). We, therefore, conduct an additional search for solutions by taking the parallax effect into account. Including the parallax effect in modeling requires us to add two more parameters $\pi_{E,N}$ and $\pi_{E,E}$, which represent the components of the microlens-parallax vector π_E projected onto the sky along the north and east equatorial coordinates, respectively. The microlens-parallax vector is related to the relative lens-source parallax $\pi_{\text{rel}} = au(D_L^{-1} - D_S^{-1})$ and the angular Einstein radius by

$$\pi_E = \frac{\pi_{\text{rel}} \mu}{\theta_E \mu}, \quad (2)$$

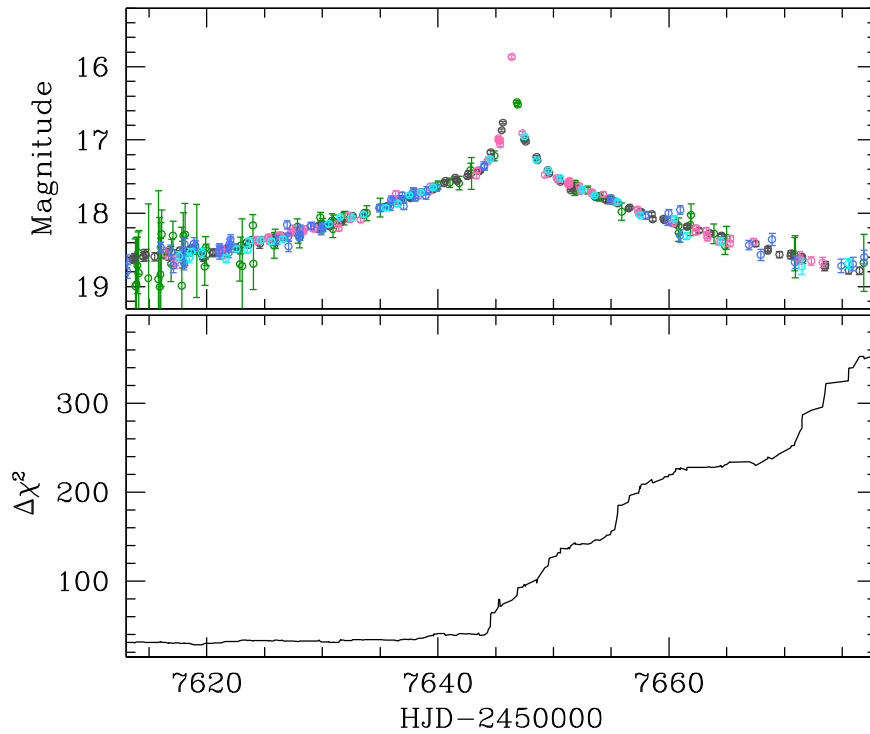


Figure 3. Cumulative distribution of $\Delta\chi^2$ between the best-fit model considering higher-order effects and the standard model. The light curve in the upper panel is presented to show the region of χ^2 difference.

Table 3
Best-fit Lensing Parameters

Parameters	$u_0 > 0$	$u_0 < 0$
t_0 (HJD')	7646.598 ± 0.035	7646.621 ± 0.034
u_0	0.052 ± 0.001	-0.051 ± 0.001
t_E (days)	99.74 ± 0.76	99.35 ± 0.84
s	0.354 ± 0.010	0.345 ± 0.011
q	0.269 ± 0.020	0.289 ± 0.029
α (rad)	-0.073 ± 0.004	0.063 ± 0.009
ρ (10^{-3})	4.48 ± 0.41	4.33 ± 0.49
$\pi_{E,N}$	0.226 ± 0.045	-0.179 ± 0.051
$\pi_{E,E}$	0.360 ± 0.013	0.367 ± 0.012
ds/dt (yr^{-1})	-0.390 ± 0.048	-0.273 ± 0.066
$d\alpha/dt$ (yr^{-1})	-0.052 ± 0.061	-0.099 ± 0.070
$(F_s/F_b)_{\text{OGLE},I}$	$0.120/0.143$	$0.119/0.143$

Note. HJD' = HJD - 2450000.

where μ represents the relative lens-source proper motion. From the modeling including the parallax effect, we find models that adequately describe the observed light curve.

Figure 2 shows the $\Delta\chi^2$ map of the MCMC chain in the $s - q$ parameter space obtained from the grid search including parallax effects. We identify two locals in the close ($s < 1$) and wide ($s > 1$) binary regimes, which are caused by the well-known close/wide degeneracy (Dominik 1999b; Bozza 2000; An 2005). The map also shows that the central anomaly in the observed light curve was produced by a binary with roughly equal mass components rather than a planetary system.

It is known that the orbital motion of a binary lens can also induce long-term deviations in lensing light curves (Dominik 1999a; Albrow et al. 2000; Park et al. 2013). We, therefore, conduct an additional modeling of the light curve taking

account of the lens-orbital effects. To the first-order approximation, the lens-orbital effect is described by two parameters ds/dt and $d\alpha/dt$, which represent the rates of change of the binary separation and the source-trajectory angle, respectively.

In Table 2, we present χ^2 values of the models that we tested. Here the “standard” model represents the solution based on the seven principle binary-lens parameters. The “parallax” model denotes the solution found by considering the parallax effect, and the “orbit+parallax” model represents the solution obtained by considering both the orbital and parallax effects. The notations “close” and “wide” denote the pair of solutions with $s < 1$ and $s > 1$, respectively. The models denoted by “ $u_0 > 0$ ” and “ $u_0 < 0$ ” represent the pair of solutions resulting from the “ecliptic degeneracy,” which is caused by the mirror symmetry of the source trajectory with respect to the binary axis (Skowron et al. 2011).

From the comparison of the models, it is found that the parallax effect significantly improves the fit, i.e., $\Delta\chi^2 = 464.5$ and 382.7 for the close and wide-binary cases, respectively. On the other hand, the improvement by additionally considering the lens-orbital effect, $\Delta\chi^2 < 5$, is meager. We also find that the close-binary solution is moderately ($\Delta\chi^2 > 10$) preferred over the wide-binary solution. However, the degeneracy between the $u_0 > 0$ and $u_0 < 0$ solutions is very severe ($\Delta\chi^2 < 1$). In Figure 1, we present the model light curve of the best-fit solution, i.e., close “orbit+parallax” model with $u_0 > 0$, plotted over the data points. For comparison, we present the residuals from the best-fit solution and the standard solution in the lower two panels. In Figure 3, we also present the cumulative distribution of $\Delta\chi^2$ between the best-fit solution and the standard model to show the region of χ^2 improvement. One finds that χ^2 improvement occurs during the central anomaly and throughout the region after the peak.

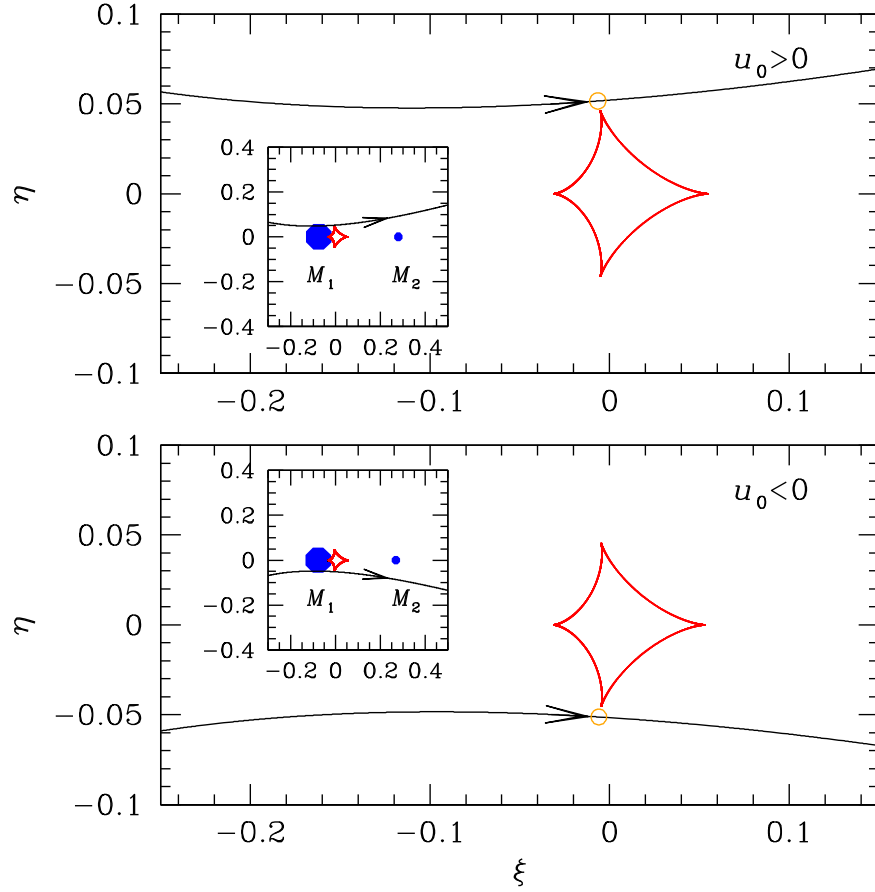


Figure 4. Geometry of the lens system. The upper and lower panels correspond to the $u_0 > 0$ and $u_0 < 0$ solutions, respectively. The coordinates (ξ, η) are centered at the barycenter of the lens system and lengths are normalized to the angular Einstein radius. The cuspy close figure represents the caustic and the curve with an arrow is the source trajectory. The small orange circle at the tip of the arrow on the source trajectory represents the source size relative to the caustic. The inset in each panel is inserted to show the caustic position with respect to the binary-lens components (marked by blue dots).

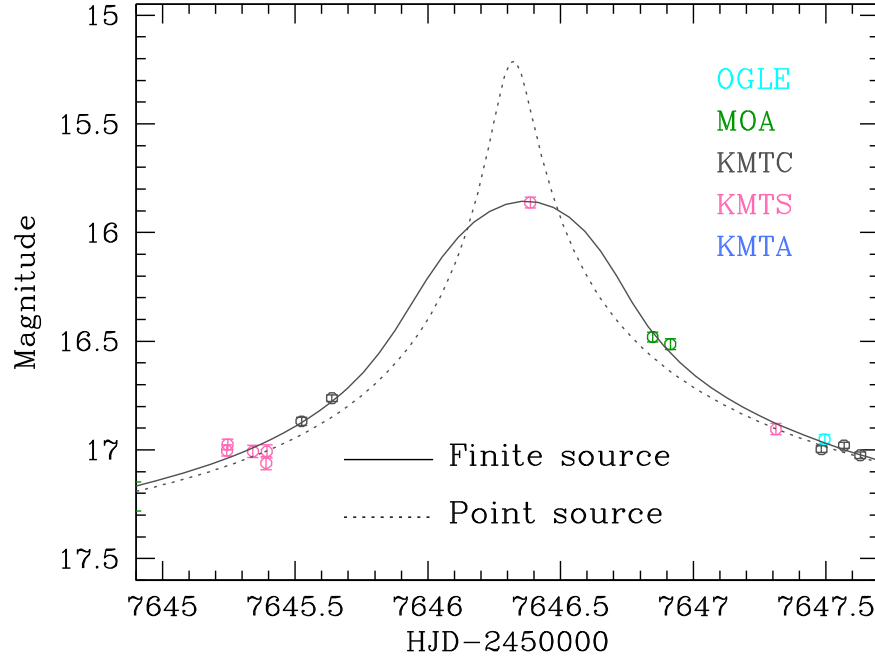


Figure 5. Model light curves around the central anomaly region resulting from a finite and a point source.

In Table 3, we present the lensing parameters of the best-fit solutions. Due to the severity of the degeneracy, we present both the $u_0 > 0$ and $u_0 < 0$ solutions. Also presented is the

fluxes from the source, F_s , and blend, F_b , that are measured in the I -band OGLE data. The uncertainty of each parameter is estimated based on the scatter of points in the MCMC chain.

In Figure 4, we present the lens system geometry, which shows the source trajectory (the curve with an arrow) with respect to the lens components (the blue dots) and caustics (the cuspy close curve). We present two cases corresponding to the $u_0 > 0$ (upper panel) and $u_0 < 0$ (lower panel) solutions. We find that the event was produced by a binary composed of two masses with a projected separation $s \sim 0.35$ and a mass ratio $q \sim 0.28$. The binary lens induced a small four-cusp caustic around the barycenter of the lens and the source star moved almost parallel to the binary-lens axis, i.e., $\alpha \sim 0$. The central anomaly was produced when the source passed the tip of the off-binary-axis cusp. Note that although the source star did not cross the caustic, finite-source effects are clearly detected. This is possible due to the steep magnification gradient in the region extending from the strong cusp of the caustic. In Figure 5, we present the two model light curves resulting from a finite (solid curve) and a point source (dotted curve). We note that the point-source light curve is based on the same lensing parameters as those of the finite-source model except ρ .

4. Physical Lens Parameters

As shown in Figure 6, where we present the $\Delta\chi^2$ distributions of MCMC chains in the $\pi_{E,E} - \pi_{E,N}$ (left panel) and $u_0 - \rho$ (right panel) parameter space, both microlens-parallax and finite-source effects are clearly detected. In this case, one can measure both $\pi_E = (\pi_{E,N}^2 + \pi_{E,E}^2)^{1/2}$ and θ_E , which are the two ingredients needed for the unique determinations of the mass M and the distance to the lens D_L , i.e.,

$$M = \frac{\theta_E}{\kappa\pi_E}; \quad D_L = \frac{\text{au}}{\pi_E\theta_E + \pi_S}. \quad (3)$$

Here $\kappa = 4G/(c^2\text{au})$, $\pi_S = \text{au}/D_S$ denotes the parallax of the source, and D_S is the distance to the source.

The angular Einstein radius is determined from the combination of the measured finite-source parameter ρ and the angular radius of the source star, θ_* , i.e., $\theta_E = \rho/\theta_*$. We determine the angular source size based on the source type deduced from the color and brightness. In order to estimate the de-reddened color $(V - I)_0$ and brightness I_0 of the source star, we use the usual method of Yoo et al. (2004), where $(V - I)_0$ and I_0 are estimated based on the offsets in color and magnitude from those of the centroid of giant clump for which the de-reddened color and brightness $(V - I, I)_{\text{GC},0} = (1.06, 14.25)$ (Bensby et al. 2011; Nataf et al. 2013) are known. Figure 7 shows the location of the source star with respect to the giant clump centroid in the instrumental color-magnitude diagram of stars in the neighboring region around the source. We note that the color-magnitude diagram is uncalibrated and thus one cannot determine the reddening $E(V - I) = (V - I) - (V - I)_0$ or the extinction $A_I = I - I_0$. However, one can measure the de-reddened color and magnitude of the source star based on the offsets $\Delta(V - I, I) = (-0.3, 3.5)$ with respect to the centroid of the giant clump. The estimated de-reddened color and magnitude of the source star are $(V - I, I)_0 = (0.8, 18.5)$ and find that the source is a mid-G-type main-sequence star. Once $(V - I)_0$ color is estimated, we convert it into $(V - K)_0 = 1.64 \pm 0.05$ using the VI/VK relation (Bessell & Brett 1988) and then estimate the source angular radius from the VK/θ_* relation (Kervella et al. 2004). The estimated angular source radius is $\theta_* = 0.94 \pm 0.07 \mu\text{as}$. The angular Einstein radius estimated

from θ_* and ρ is

$$\theta_E = \begin{cases} 0.21 \pm 0.03 \text{ mas} & \text{for } u_0 > 0, \\ 0.22 \pm 0.03 \text{ mas} & \text{for } u_0 < 0. \end{cases} \quad (4)$$

With the measured timescale, then, the relative lens-source proper motion is estimated by $\mu = \theta_E/t_E$. We find that

$$\mu = \begin{cases} 0.87 \pm 0.10 \text{ mas yr}^{-1} & \text{for } u_0 > 0, \\ 0.81 \pm 0.11 \text{ mas yr}^{-1} & \text{for } u_0 < 0. \end{cases} \quad (5)$$

We note that the measured relative proper motion is substantially smaller than $\sim 5 \text{ mas yr}^{-1}$ of typical Galactic lensing events. We discuss the probability of low proper motions in Section 5.

In Table 4, we present the estimated physical lens parameters. Here M_1 and M_2 denote the masses of the lens components, $a_\perp = sD_L\theta_E$ is the physical size of the projected separation between the lens components, and $(\text{KE}/\text{PE})_\perp$ denotes the transverse kinetic-to-potential energy ratio that is defined by (Dong et al. 2009)

$$\left(\frac{\text{KE}}{\text{PE}}\right)_\perp = \frac{(a_\perp/\text{au})^3}{8\pi^2(M/M_\odot)} \left[\left(\frac{1}{s} \frac{ds}{dt} \right)^2 + \left(\frac{d\alpha}{dt} \right)^2 \right]. \quad (6)$$

This ratio is less than the three-dimensional kinetic-to-potential energy ratio, KE/PE , which is less than unity for a bound system, i.e., $(\text{KE}/\text{PE})_\perp < \text{KE}/\text{PE} < 1$. We find that both lens components have masses below the hydrogen-burning limit of $\sim 0.08 M_\odot$, indicating that the lens is a brown-dwarf binary. This is the third microlensing brown-dwarf binary followed by the first discoveries of OGLE-2009-BLG-151L and OGLE-2011-BLG-0420L by Choi et al. (2013). The brown-dwarf binary is located at a distance $D_L \sim 4.5 \text{ kpc}$ from the Earth. The projected separation between the binary components is $a_\perp = 0.33 \text{ au}$ and 0.34 au for the $u_0 > 0$ and $u_0 < 0$ solutions, respectively.

5. Discussion

As mentioned in the previous section, the measured relative lens-source proper motion $\mu \sim 0.8\text{--}0.9 \text{ mas yr}^{-1}$ is substantially smaller than $\sim 5 \text{ mas yr}^{-1}$ of typical Galactic lensing events. Tracking down the cause of the low μ value is important because μ is estimated from θ_E and thus a wrong θ_E determination can lead to erroneous determinations of the other physical lens parameters.

In order to trace the origin of the estimated low proper motion, we conduct a Monte Carlo simulation of Galactic microlensing events based on the models of physical and dynamical distributions of the Galaxy combined with the mass function of objects. We adopt the Galactic model of Han & Gould (1995) for the physical and dynamical distributions of matter. In this model, the disk matter distribution is modeled by a double-exponential disk and the velocity distribution is assumed to be Gaussian about the rotation velocity. The bulge is modeled by a triaxial bulge and matter in the bulge moves following a triaxial Gaussian distribution, where the velocity components along the major axes are deduced from the flattening of the bulge via the tensor virial theorem. For the mass function of lens objects, we adopt the Gould (2000) model, which is constructed based on a stellar luminosity function plus stellar remnants. Based on the models, we

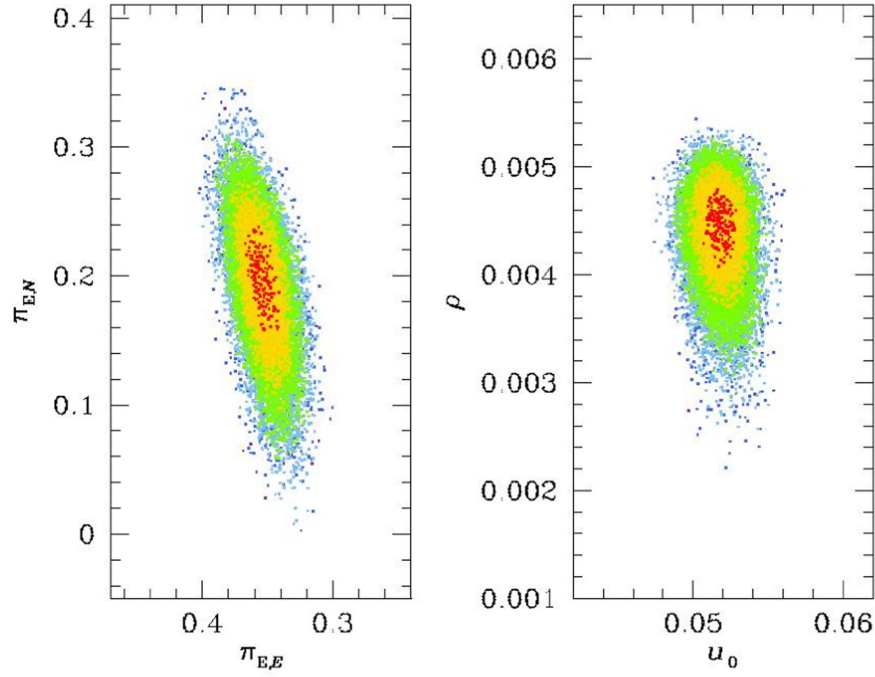


Figure 6. $\Delta\chi^2$ distributions of MCMC chains in the $\pi_{E,E}$ – $\pi_{E,N}$ (left panel) and u_0 – ρ (right panel) parameter space. Different colored dots represent chains with $\Delta\chi^2 < 1$ (red), 4 (yellow), 9 (green), 16 (cyan), and 25 (blue).

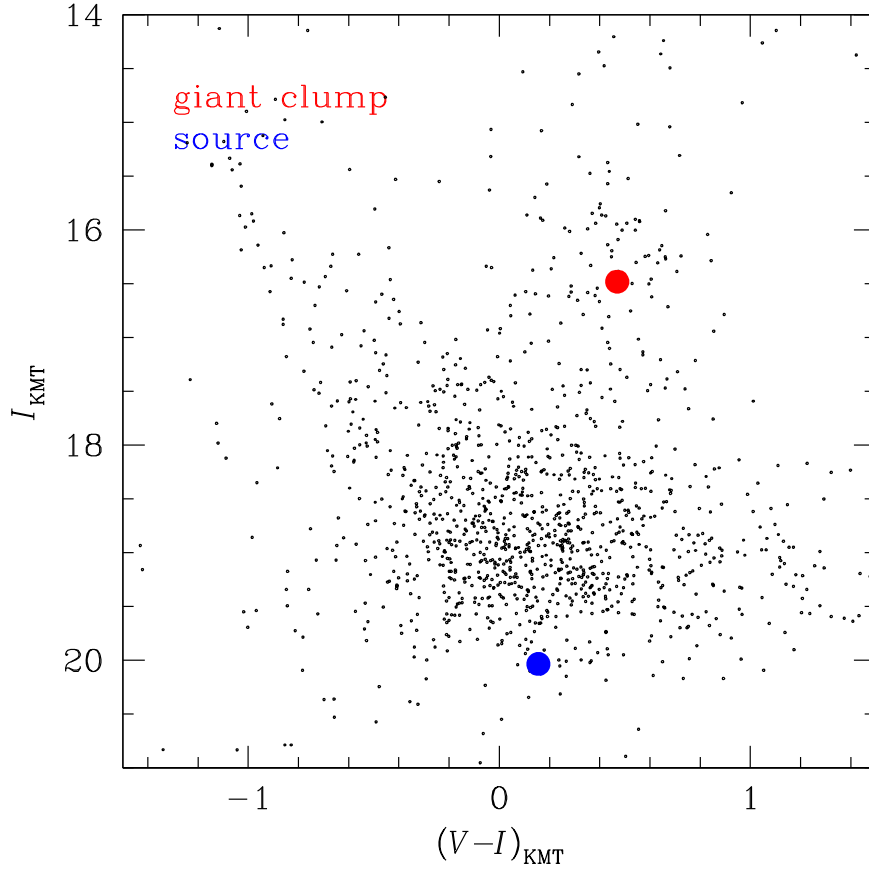


Figure 7. Position of the source star with respect to the centroid of the giant clump in the instrumental color–magnitude diagram.

produce a large number (10^5) of mock events and compute timescales and proper motions of events.

In Figure 8, we present the distributions of relative lens–source proper motions obtained from the simulation. To see the

variation of the proper-motion distribution $f(\mu)$ depending on the event timescale, we produce distributions for three different populations of events: (1) all events, (2) events with timescales $t_E > 50$ days, and (3) those with $t_E > 100$ days. From the

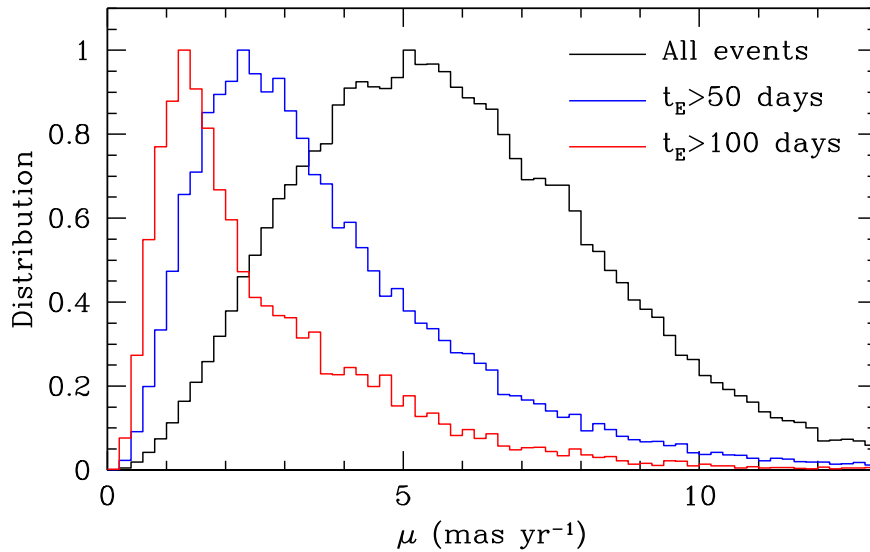


Figure 8. Distributions of relative lens-source proper motion for three different populations of Galactic lensing events: all events (black curve), events with $t_E > 50$ days (blue curve), and those with $t_E > 100$ days.

Table 4
Physical Lens Parameters

Parameter	Model	
	Close	Wide
$M_1 (M_\odot)$	0.048 ± 0.007	0.051 ± 0.008
$M_2 (M_\odot)$	0.013 ± 0.002	0.015 ± 0.002
D_L (kpc)	4.47 ± 0.51	4.48 ± 0.51
a_\perp (au)	0.33 ± 0.04	0.34 ± 0.04
$(KE/PE)_\perp$	0.01	0.01

presented distributions, it is found that the proper-motion distributions show a trend where the mode value of the μ distribution becomes smaller as the event timescale increases. As expected, the mode value of all Galactic lensing events is $\mu \sim 5 \text{ mas yr}^{-1}$. However, the relative proper motion becomes smaller with the increase of the event timescale. It is found that the mode value of the distributions are $\mu \sim 2.3 \text{ mas yr}^{-1}$ and $\sim 1.2 \text{ mas yr}^{-1}$ for events with $t_E > 50$ days and > 100 days, respectively. Considering that the timescale of OGLE-2016-BLG-1469 is ~ 100 days, the measured proper motion of $\mu \sim 0.8\text{--}0.9 \text{ mas yr}^{-1}$ is not an abnormally small value but a typical value for long timescale events.

Being able to detect brown-dwarf binaries that are difficult to detect with other methods, microlensing is a complementary method to other methods. The majority of nearby brown-dwarf binaries discovered by direct imaging have separations in the range of 1 to 10 au. See the histogram of projected separations presented in Figure 2 of Aller (2012). Microlensing sensitivity is maximum for binaries separated by the Einstein radius, which is related to the mass and distance of the binary by

$$r_E \sim 0.9 \text{ au} \left(\frac{M_{\text{tot}}}{0.05 M_\odot} \right)^{1/2} \left(\frac{D_S}{8 \text{ kpc}} \right)^{1/2} \left[\frac{x(1-x)}{0.25} \right]^{1/2}, \quad (7)$$

where $x = D_L/D_S < 1.0$. Therefore, microlensing is sensitive to close brown-dwarf binaries with separations $a_\perp \lesssim 1 \text{ au}$, for which the sensitivities of other methods are low. Actually, the projected separations of the three microlensing brown-dwarf

binaries are $a_\perp \sim 0.3 \text{ au}$, 0.2 au , and 0.3 au for OGLE-2009-BLG-151L, OGLE-2011-BLG-0420L, and this system, respectively. The mass ratio histogram of brown-dwarf binaries discovered by direct imaging (Aller 2012) exhibits a clear tendency of equal mass systems. The lack of low-mass ratio systems is likely to be due to the difficulty in detecting second components. By contrast, the dependency of the microlensing sensitivity to the mass ratio is weak and the efficiency extends down to planetary companions with $q < 0.1$, e.g., OGLE-2012-BLG-0358Lb (Han et al. 2013). There exist multiple theories for the formation of binary brown dwarfs, e.g., Reipurth & Clarke (2001), Stamatellos & Whitworth (2009), and Bate (2009). These different formation mechanisms would result in different binary properties such as binary frequency, mass ratios, and separations. Therefore, a sample comprising brown-dwarf binaries with physical parameters spanning wide ranges is important to better understand the formation mechanism of binary brown dwarfs.

6. Conclusion

We reported the microlensing discovery of a binary that was composed of two brown dwarfs. The brown-dwarf binary was found from the analysis of the microlensing event OGLE-2016-BLG-1469. The light curve of the event exhibited a short-term central anomaly, which turned out to be produced by a binary companion with a mass roughly equal to the primary. Although the source star did not cross the caustic induced by the binary companion, finite-source effects were clearly detected, enabling us to measure the angular Einstein radius. In addition, we measured the microlens parallax from the asymmetric light curve. By measuring both the angular Einstein radius and the microlens parallax, we could uniquely determine the masses and identified the substellar nature of the lens components. The lens was the third microlensing brown-dwarf binary with measured mass, demonstrating the usefulness of the microlensing method in detecting field brown-dwarf binaries.

Work by C. Han was supported by the the grant 2017R1A4A1015178 of National Research Foundation of Korea. The OGLE project has received funding from the National Science Centre, Poland, grant MAESTRO 2014/14/A/ST9/00121 to A. Udalski. OGLE Team thanks Profs. M. Kubiak, G. Pietrzyński, and Ł. Wyrzykowski for their contribution to the collection of the OGLE photometric data over the past years. The MOA project is supported by JSPS KAKENHI Grant Numbers JP24253004, JP26247023, JP16H06287, JP23340064, and JP15H00781. Work by A. Gould was supported by JPL grant 1500811. A. Gould and W. Zhu acknowledge the support from NSF grant AST-1516842. Work by J.C. Yee. was performed under contract with the California Institute of Technology (Caltech)/Jet Propulsion Laboratory (JPL) funded by NASA through the Sagan Fellowship Program executed by the NASA Exoplanet Science Institute. This research has made use of the KMTNet system operated by the Korea Astronomy and Space Science Institute (KASI) and the data were obtained at three host sites of CTIO in Chile, SAAO in South Africa, and SSO in Australia. We acknowledge the high-speed internet service (KREONET) provided by Korea Institute of Science and Technology Information (KISTI).

References

- Alard, C., & Lupton, R. H. 1998, *ApJ*, **503**, 325
- Albrow, M. D., Beaulieu, J.-P., Caldwell, J. A. R., et al. 2000, *ApJ*, **534**, 894
- Albrow, M. D., Horne, K., Bramich, D. M., et al. 2009, *MNRAS*, **397**, 2099
- Aller, K. N. 2012, in Proc. IAU Symp. 282, From Interacting Binaries to Exoplanets: Essential Modeling Tools, ed. M. T. Richards & I. Hubeny (Cambridge: Cambridge Univ. Press), 105
- An, J. H. 2005, *MNRAS*, **356**, 1409
- An, J. H., & Han, C. 2002, *ApJ*, **573**, 351
- Basri, G. 2000, *ARA&A*, **38**, 485
- Bate, M. R. 2009, *MNRAS*, **392**, 590
- Bensby, T., Adén, D., Meléndez, J., et al. 2011, *A&A*, **533**, 134
- Bessell, M. S., & Brett, J. M. 1988, *PASP*, **100**, 1134
- Bond, I. A., Abe, F., Dodd, R. J., et al. 2001, *MNRAS*, **327**, 868
- Bozza, V. 2000, *A&A*, **355**, 423
- Burgasser, A. J., Sheppard, S. S., & Luhman, K. L. 2013, *ApJ*, **772**, 129
- Choi, J.-Y., Han, C., Udalski, A., et al. 2013, *ApJ*, **768**, 129
- Claret, A. 2000, *A&A*, **363**, 1081
- Dominik, M. 1999a, *A&A*, **329**, 361
- Dominik, M. 1999b, *A&A*, **349**, 108
- Dong, S. S., Gould, A., Udalski, A., et al. 2009, *ApJ*, **695**, 970
- Gould, A. 1992, *ApJ*, **392**, 442
- Gould, A. 2000, *ApJ*, **535**, 928
- Gould, A. 2008, *ApJ*, **681**, 1593
- Griest, K., & Safizadeh, N. 1998, *ApJ*, **500**, 37
- Han, C., & Gould, A. 1995, *ApJ*, **447**, 53
- Han, C., Jung, Y. K., Udalski, A., et al. 2013, *ApJ*, **778**, 38
- Kervella, P., Thévenin, F., Di Folco, E., & Ségransan, D. 2004, *A&A*, **426**, 297
- Kim, S.-L., Lee, C.-U., Park, B.-G., et al. 2016, *JKAS*, **49**, 37
- Luhman, K. L. 2013, *ApJL*, **767**, L1
- Nakajima, T., Oppenheimer, B. R., Kulkarni, S. R., et al. 1995, *Natur*, **378**, 463
- Nataf, D. M., Gould, A., Fouqué, P., et al. 2013, *ApJ*, **769**, 88
- Park, H., Udalski, A., Han, C., et al. 2013, *ApJ*, **778**, 134
- Pejcha, O., & Heyrovský, D. 2009, *ApJ*, **690**, 1772
- Rebolo, R., Zapatero Osorio, M. R., & Martí, E. L. 1995, *Natur*, **377**, 129
- Reipurth, B., & Clarke, C. 2001, *AJ*, **122**, 432
- Skowron, J., Udalski, A., Gould, A., et al. 2011, *ApJ*, **738**, 87
- Stamatellos, D., & Whitworth, A. P. 2009, *MNRAS*, **392**, 413
- Sumi, T., Abe, F., Bond, I. A., et al. 2003, *ApJ*, **591**, 204
- Tomaney, A. B., & Crots, A. P. S. 1996, *AJ*, **112**, 2872
- Udalski, A. 2003, *AcA*, **53**, 291
- Udalski, A., Szymański, M. K., & Szymański, G. 2015, *AcA*, **65**, 1
- Yee, J. C., Shvartzvald, Y., Gal-Yam, A., et al. 2012, *ApJ*, **755**, 102
- Yoo, J., DePoy, D. L., Gal-Yam, A., et al. 2004, *ApJ*, **603**, 139
- Zapatero Osorio, M. R., Lane, B. F., Pavlenko, Y., et al. 2004, *ApJ*, **615**, 958